Intramural Multisite Recording of Transmembrane Potential in the Heart

Darren A. Hooks,* Ian J. LeGrice,* John D. Harvey,† and Bruce H. Smaill*
*Department of Physiology, School of Medicine, and †Department of Physics, University of Auckland, Auckland, New Zealand

ABSTRACT Heart surface optical mapping of transmembrane potentials has been widely used in studies of normal and pathological heart rhythms and defibrillation. In these studies, three-dimensional spatio-temporal events can only be inferred from two-dimensional surface potential maps. We present a novel optical system that enables high fidelity transmural recording of transmembrane potentials. A probe constructed from optical fibers is used to deliver excitation light and collect fluorescence from seven positions, each 1 mm apart, through the left ventricle wall of the rabbit heart. Excitation is provided by the 488-nm line of a water-cooled argon-ion laser. The fluorescence of the voltage-sensitive dye di-4-ANEPPS from each tissue site is split at 600 nm and imaged onto separate photodiodes for later signal ratioing. The optics and electronics are easily expandable to accommodate multiple optical probes. The system is used to record the first simultaneous measurements of transmembrane potential at a number of sites through the intact heart wall.

INTRODUCTION

The first intramural recordings of cardiac electrical activation were made by Durrer and van der Tweel (1953). They used purpose-built hypodermic needle probes with which extracellular potentials were measured at sites along the needle via ultra-fine wires introduced through its lumen. Their technique has since been used by a number of investigators (Selvester et al., 1970; Kerber et al., 1994; Sands et al., 1999). By increasing the number of needles inserted through the heart wall, the transmural spread of electrical activation has been mapped in three dimensions, revealing details of normal and arrhythmic propagation (Chen et al., 1988; Frazier et al., 1988; Arnar et al., 1997).

There are problems, however, in relating extracellular potential signals to underlying cellular electrical activity. Extracellular signals represent the integrated effects of membrane currents over a relatively large volume, and distinguishing near from far electrical events is often difficult. As a consequence, activation and recovery, the two most basic characteristics of propagation, cannot be identified reliably at the site of recording for conditions other than uniform propagation (Steinhaus, 1989).

Over the past two decades, optical measurement of transmembrane potential has provided an increasingly attractive option for cardiac electrical mapping studies. Optical mapping has distinct advantages over extracellular techniques. Foremost is the ability to interrogate cellular propagation directly by imaging transmembrane potentials. With optical mapping it is possible to achieve high spatial resolution. It is also possible to map potentials during the application of defibrillating shocks to the heart, when conventional electrical measurement techniques cannot be used. To date, however, optical measurement of transmembrane potential has been almost entirely restricted to the heart surfaces. The ability to access deeper propagation processes has in general been limited by scattering and absorption of the voltage-dependent fluorescence signal (Girouard et al., 1996). Recently, electrical activity inside cardiac muscle has been visualized via fluorescence measurements made in a transillumination mode (Baxter et al., 2001). This technique currently offers a low degree of spatial resolution through the wall of the heart however and is not applicable to the study of intact heart preparations.

We have developed a novel optical system for measuring intramural cardiac action potentials. Our main objectives were to record ventricular membrane potentials at sites with transmural separation comparable with extracellular needle probes, using a system that could readily be expanded to map the three-dimensional spread of electrical activation through the ventricular wall. These objectives were met with the design 1) of a robust, small diameter, optical probe (optrode) able to deliver and collect light deep within tissue and 2) of a modular (scalable) recording complex capable of simultaneous measurement of fluorescence signals and extracellular potentials. Dual wavelength collection of di-4-ANEPPS emission was used to reduce light source noise and motion-related artifact, in a ratiometric fashion similar to that reported by Knisley et al. (2000).

METHODS

Optics

A schematic representation of the optical system is given in Fig. 1 *A*. Excitation light (488 nm) from a water-cooled argon ion laser (Spectra Physics; model 165) was delivered to separate tissue sites via a fiber optic conduit that terminated in a purpose-built optical probe *(*optrode*)*. Fluorescence collected from each site returned through the "tissue" conduit and was split into two frequency bands. Long and short wavelengths were routed to discrete photodiodes via separate fiber optic "detector" conduits. Aspects of the optical design are similar to the tissue culture imaging system of Rohr and Kucera (1998).

Received for publication 28 August 2000 and in final form 3 July 2001.

Address reprint requests to Darren A. Hooks, Department of Physiology, School of Medicine, University of Auckland, Private Bag 92019, Auckland, New Zealand. Tel.: 64-9-373-7599; Fax: 64-9-373-7499; E-mail: d.hooks@auckland.ac.nz.

0006-3495/01/11/2671/10 $2.00

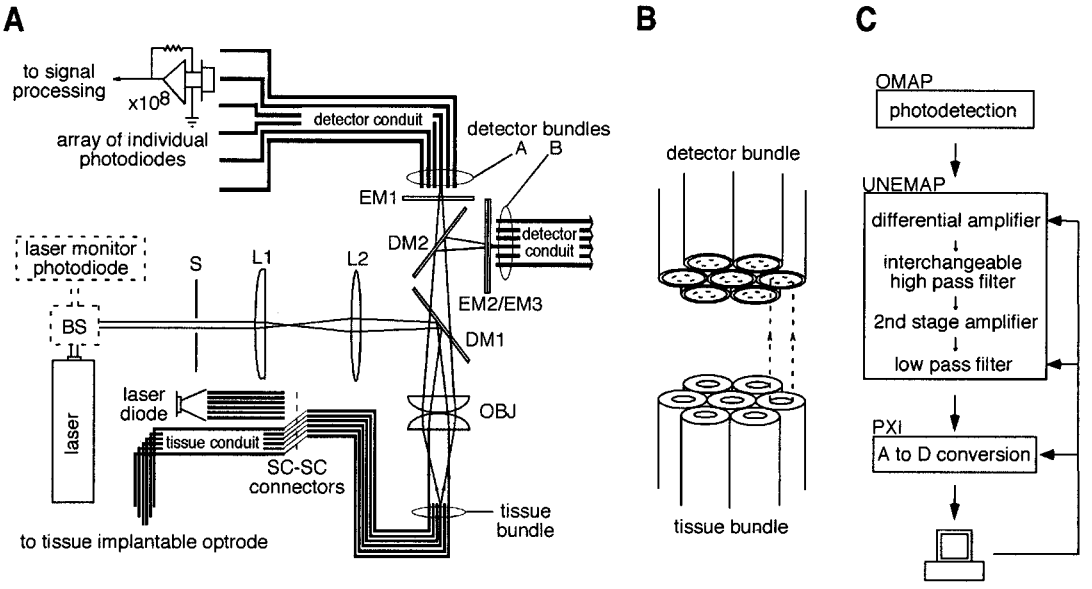

FIGURE 1 (*A*) Schematic overview of the optical layout. See text for detailed description. L1 and L2, focal length 50- and 80-mm converging lenses; OBJ, 10× microscope objective; DM1 and DM2, 520- and 600-nm-long pass dichroic mirrors; EM1 and EM2, 600- and 520-nm-long pass emission filters; EM3, 600-nm-short pass emission filter; S, shutter; BS, beam steerer. (*B*) Schematic of the coupling of fluorescence from the tissue bundle to a detector bundle. The fibers of the detector bundles have an increased ratio of core:outer diameter, which leads to greater coupling efficiency and easier alignment. For simplicity the objective lens has been omitted. (*C*) Schematic overview of the system electronics. Design is based around the three units: OMAP, UNEMAP, PXI (see text for details). Arrows to and from the computer represent data input and digital control lines, respectively.

Each conduit consisted of seven optical fibers. These were packed in hexagonal bundles toward the center of the optical system to optimize coupling of excitation light into the tissue conduit and fluorescence emission into the detector conduits. The central ends of the fiber optic conduits are subsequently referred to as the "tissue bundle" and "detector bundles A and B."

The tissue bundle was formed within an SMA type fiber-optic connector (Thorlabs Inc., Newton, NJ), and mounted in a multimode fiber coupler (F-91-C1-T; Newport Corporation, Irvine, CA), which allowed *xyz* positioning as well as rotation about the bundle central axis. The detector bundles were mounted in fiber optic positioners attached to translation stages (FP-1, Model 426; Newport Corporation) for accurate placement. The end faces of all fiber bundles were manually polished.

Light from the laser was coupled into the tissue bundle by the lenses L1 and L2, a 520-nm long-pass dichroic mirror (DM1), and a 10× microscope objective (OBJ). Beam diameter was varied, to ensure optimal coupling to tissue bundles of various dimensions, by adjusting the distances L1-L2 and L2-OBJ. The lenses and objective were positioned so that the laser beam was in all cases collimated at the face of the tissue bundle.

The tissue bundle was imaged onto the detector bundles via the objective OBJ. Return fluorescence was split by the 600-nm long-pass dichroic mirror (DM2) and further band-limited by the emission filters EM1(>600 nm) and EM2/EM3 (520–600 nm). Each detector fiber terminated with an SMA connector for coupling to the photodetection system.

Optimal mapping of the tissue bundle image onto the detector bundles was achieved as follows. The optrode was immersed in a fluorescent solution and the ratio $\Sigma A_i/\Sigma B_i$ was monitored continuously. A_i and B_i are the fluorescence levels recorded through individual fibers of detector conduits A and B. First, detector bundle B was fixed in position, and detector bundle A was adjusted to maximize $\Sigma A_i/\Sigma B_i$. Detector bundle B was then moved, with bundle A fixed until the ratio reached a minimum. The use of this ratiometric approach in the alignment procedure enabled us to reduce errors due to bleaching of the fluorescence signal and laser power fluctuation.

Cross-talk (defined as the fraction of total detected fluorescence power from any tissue fiber detected by photodiodes not assigned to that fiber) was used as a measure of the effectiveness of optical coupling in the system. Ideally, there should be one to one mapping between tissue fibers and associated detector fibers. However, cross-talk may arise from the diffraction limitations of the objective lens, different bundle geometries, or from bundle misalignments. Cross-talk could not easily be determined with the optrode attached to the tissue bundle. A join was therefore added to the tissue conduit with a series of SC-SC type fiber connectors (Thorlabs Inc.) so that cross-talk could be evaluated by reverse illumination of individual fibers in the tissue conduit with a laser diode.

Optrode

The distal end of the tissue conduit formed the optrode. The buffer coatings of the conduit fibers were removed at the optrode end to reduce their size. Fibers were then hexagonally arranged and terminated at 1-mm intervals (Fig. 2). The end of each fiber was polished at 40° to its longitudinal axis to produce total internal reflection of excitation light and collected fluorescence at this face. A glass-air interface is required for total internal reflection, and for this reason the fibers were loaded into a glass micropipette plugged with epoxy resin at its tip. This construction also adds strength to the probe and aids in cleaning after experiments. Fibers were oriented so that excitation light was emitted radially from the optrode: the principal direction of emission (and collection) for successive fibers being separated by 60° to minimize reflective losses at the micropipette surfaces. The micropipette was pulled manually to a gradual taper to ease insertion into the tissue. The total diameter of the optrode was ~400 μm. Fig. 2 shows the pattern of illumination obtained when three of the seven optical fibers of the optrode were illuminated during immersion in a dilute solution of sulforhodamine B.

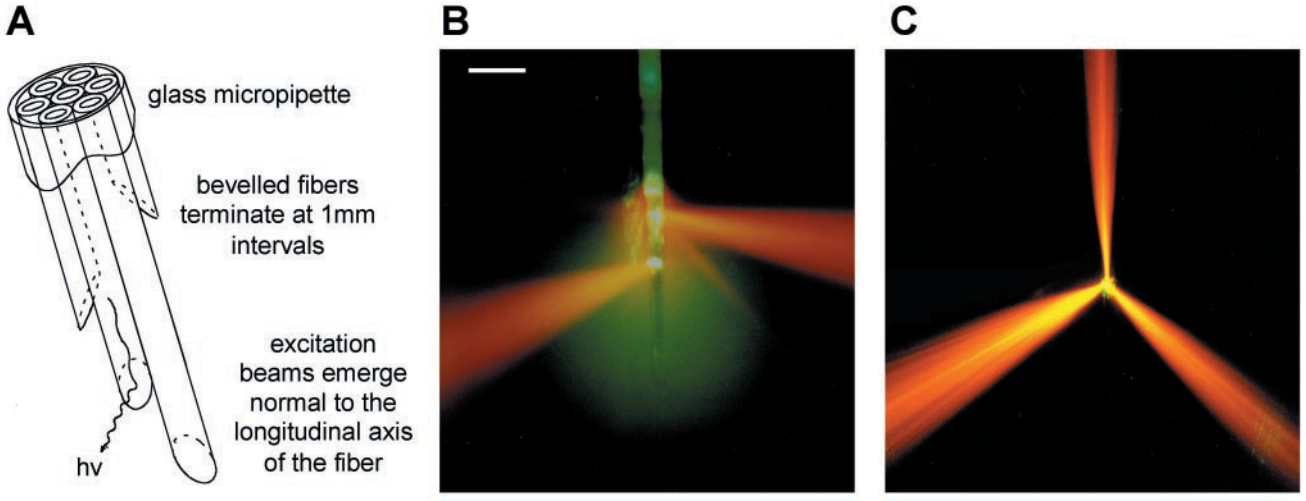

FIGURE 2 (*A*) Schematic of the tissue implantable optrode (not drawn to scale). Seven optical fibers are arranged in a hexagonal array, and terminate at 1-mm intervals. All fibers are enclosed in a glass micropipette. Light emission is from the side of the fibers by total internal reflection off their bevelled ends. (*B* and *C*) Photographs of the optrode in side and end-on views. Optrode is immersed in a fluorescing rhodamine solution. The green halo surrounding the optrode in *B* is caused by reflection of the beam that propagates into the page. For illustrative purposes only three of the seven optrode fibers carry excitation light. Scale bar = 2 mm (*B*).

Optical fibers

Separate tissue conduits were fabricated to compare the performance of two different types of optical fiber: GIF625 (Thorlabs Inc) (GIF625 is a standard communication graded index fiber) and F-MCB-T (Newport Corp). FT-1.0-EMT fibers (Thorlabs Inc) were used for the detection conduits. Specifications for all three optical fibers are given in Table 1. A water-clear optical epoxy (Epoxies Etc, Cranston, RI) was used to bond the hexagonally packed fiber bundle at the proximal end of the tissue conduit. Nontransparent epoxies did not remain intact when exposed to the intense laser beam.

The outer diameter of the detector fibers determines the magnification required to match the image of the tissue bundle to the detector bundle. In principle, alignment safety factors and imaging efficiency should be increased if tissue fibers with a small core to outer diameter ratio are mapped onto detector fibers with a much larger core to outer diameter ratio (Fig. 1 *B*). On the other hand, the efficiency of coupling of excitation light into the tissue bundle will decrease markedly if core to outer diameter ratio is reduced. The buffer coating of the proximal ends of the GIF625 tissue fibers and the detector fibers (but not the F-MCB-T tissue fibers) was removed over the first 100 mm to achieve appropriate core to outer diameter ratios (Table 1). The ratio for the F-MCB-T fiber was most appropriate with the buffer coating left intact. However, leaving the buffer intact on this fiber lead to unforeseen contamination of the tissue fluorescence with fluorescence from the buffer coating. To overcome this problem while retaining the desired ratio, only the first 2 mm of the buffer was etched from the F-MCB-T fibers. This shifted the buffer fluorescence away from the focal plane of the large core fibers. The etching was carried out with concentrated sulfuric acid at 140°C.

Signal acquisition and processing

The acquisition system consists of three modules as illustrated in Fig. 1 *C*. In the photodetection module, SMA connectors were used to couple detector fibers directly to photodiodes (S2386-44K; Hamamatsu Photonics, Hamamatsu, Japan) mounted in columns on the front panels of the unit. The photodiodes were connected to current-voltage converters (gain = 10^8 V/A), (OPA121KU; Burr-Brown, Dallas, TX).

The photodetection system was interfaced with a multi-channel signal conditioning complex (UNEMAP; Auckland Uniservices Ltd, Auckland), which provided programmable gain (1–1100), and a 5-pole programmable low-pass filter (50 Hz to 4950 Hz). Optical signals were low-pass filtered at 500 Hz to prevent aliasing. Optional high-pass filtering (0.05 Hz) was available for the recording of extracellular potential signals.

Data was acquired with 16-bit resolution at 1.2 kHz per channel using a National Instruments™ PXI acquisition system. This consisted of four 64-channel PXI-6031E acquisition cards in a PXI-1000B chassis controlled by a master SGI 02 (Silicon Graphics Inc., Mountain View, CA) computer workstation. Data acquired by the PXI system was transferred to the SGI workstation for further processing and display.

TABLE 1 Optical fiber specifications and characteristics

Bundle	Name	Type	Diameter (μm)			Core: outer diameter ratio	Excitation efficiency (%)	Cross-talk mean (SD) (%)
			Core	Cladding	Buffer			
Tissue	GIF625	Graded index	62.5	125*	250	0.5	4	1.79 (1.47)
	F-MCB-T	Step index	100	110	140*	0.71	26	0.39 (0.13)
Detector	FT-1.0-EMT	Step index	1000	1035*	1400	0.97		

GIF625 and F-MCB-T were the fibers trialed in the tissue conduits, whereas FT-1.0-EMT was used in the detector conduits.
The fiber outer diameter (*) was the cladding diameter in cases where the buffer coating was removed. Use of F-MCB-T enabled greater excitation pathway efficiency. Cross-talk for the F-MCB-T bundle was lowest due to its more regular bundle geometry.

Each recorded signal consisted of the following components

$$= \text{tissue signal} + \text{fiber signal}$$

$$= A[V_m(t)I(t)V(t)C(t) + I(t)V(t)C(t)] + BI(t)$$

in which $V_m(t)$ is the membrane potential, $I(t)$ the laser intensity, $V(t)$ the volume of recording, $C(t)$ the concentration of fluorochrome, and A and B are constants. The fiber signal was small in comparison to the tissue signal and arose from laser light reflected off the polished tissue bundle (a small fraction of which leaked to the detectors), and fiber generated fluorescence. Before an experiment the constant B was determined for each channel with the optrode held in air. The laser intensity $I(t)$ was monitored continuously with a single photodiode (Fig. 1 *A*). This recording of laser power typically showed peak-to-peak fluctuations of up to 1.1% of total laser power. The recording was scaled and used to subtract the fiber signal component from each recording made in the heart tissue. Subsequently, the pair of signals generated from each recording site (520–600 nm and >600 nm) were ratioed.

Experimental preparation

The optical recording system was tested on Langendorff-perfused rabbit hearts ($n = 3$). All procedures were approved by the University of Auckland Animal Ethics Committee under approval N805. New Zealand White Rabbits (2.5–6 kg) were anesthetized with saffan and their hearts rapidly excised. Hearts were perfused with Kreb's solution containing 120 mM NaCl, 4.7 mM KCl, 1.2 mM KH_2PO_4, 1.2 mM $MgSO_4$, 11 mM D-glucose, 25 mM $NaHCO_3$, 1.8 mM $CaCl_2$, bubbled with 95%/5% O_2/CO_2 at an aortic pressure of 100 mm Hg, and a temperature of 37°C. The heart was stained with recirculating di-4-ANEPPS at 20 μM, for 10 min and left to equilibrate for a further 10 min. The optrode was then inserted into the free wall of the left ventricle (LV) at an angle (~20° to the epicardium), which allowed all recording sites to be located intramurally. Each optrode fiber delivered 10 mW of excitation power to the heart tissue. To investigate the efficacy of signal ratioing in the reduction of motion artifact, recordings were made with and without the addition of 2,3-butanedione monoxime (2,3-BDM, 15 mM) to the perfusate, in two hearts. All recordings in the third heart were made with 2,3-BDM. The heart was paced at the base of the right ventricle at 1.5 times threshold during recordings, and the electrical function of the heart was monitored using a bipolar epicardial electrode placed as close as practical to the optrode insertion site.

RESULTS

System efficiencies

The major losses in the excitation optical pathway occurred at the face of the tissue bundle. Fig. 3 *A* shows the tissue bundle illuminated by a segment of the laser beam. The beam intensity has a two-dimensional Gaussian density distribution

$$f(r) = \frac{1}{2\pi\sigma^2} e^{-\frac{1}{2}\left(\frac{r}{\sigma}\right)^2}$$

in which r is the radius from the center of the beam, and σ is the standard deviation (SD) of the beam intensity profile. The fraction of the laser beam that falls on the fiber cores of the tissue bundle can be estimated by evaluating the integral

$$\int\int f(r)drrd\theta$$

between the limits set by the fiber dimensions.

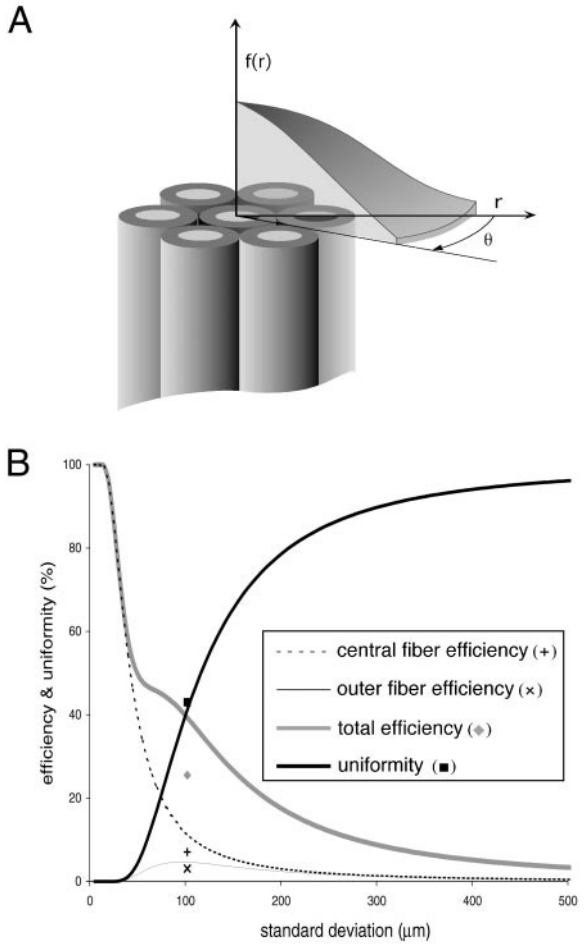

FIGURE 3 (*A*) The Gaussian distribution of laser beam intensity, superimposed on the tissue fiber bundle. (*B*) Transmission characteristics for the F-MCB-T fiber bundle. Data lines represent the results of numerical integration of the laser beam intensity profile. As the beam SD is increased from 15 μm, coupling efficiency to the central fiber diminishes, whereas coupling to the outer fibers increases to peak at a SD of 100 μm. Data points show the transmission efficiencies as determined by fiber bundle input and output beam intensity measurements.

This equation was numerically evaluated with increasing beam SD. Results for the F-MCB-T fiber bundle are presented in Fig. 3 *B*. As expected, the total efficiency of coupling of the laser beam to the tissue bundle reduces as beam diameter is expanded, whereas the uniformity of coupling to all seven fibers in the bundle is increased. Efficiency is defined as the percent of total laser power incident to the bundle that may be coupled into the fiber cores, whereas uniformity is defined as the ratio of average power carried by the outer fibers to the power carried by the central fiber. Coupling efficiency for the outer fibers of the bundle peaks at a beam SD of ~100 μm, and this is the beam SD currently used. The total loss of laser power associated with coupling into the tissue bundle and propagation through the tissue fibers can be measured directly for this beam SD. Results are shown as single data points in Fig. 3 *B*. It is evident

that there are significant losses, additional to those due to illumination of noncore parts of the tissue bundle. A major fraction of this loss is likely due to degradation of the surface polish at the face of the bundle, caused by the acid etching of the F-MCB-T fiber buffer. Theoretical losses through the fibers themselves are low (0.014dB/m). The overall efficiency of the excitation pathway, including losses through the coupling lenses, is shown in Table 1 for both types of tissue fiber. It is seen that use of the F-MCB-T fiber considerably increases the excitation efficiency of the system, and for this reason it was the fiber used in all animal experiments.

Fiber bundle alignment

The low cross-talk for both GIF625 and F-MCB-T tissue bundles (Table 1) indicates precise bundle-to-bundle imaging. Furthermore, for both fiber types, the detector bundle alignment procedures outlined in the Methods section produced optimal alignment of every fiber within the bundles (data not shown).

Fluorescence collection characteristics of the optrode

We characterized the depth over which fluorescence was collected in a single optrode fiber with the optrode placed in a rhodamine solution to ascertain whether an optrode fiber would integrate fluorescence from a similar volume as a flat-cleaved fiber. The protocol used is shown schematically in Fig. 4 *A*. Both the flat-cleaved fiber and the optrode were mounted on micromanipulators, and the fluorescence signal level detected through the fibers was recorded as they were moved away from either the base or side (Fig. 4 *A*) of a cuvette. Recordings were used to reconstruct the graph of Fig. 4 *B*. The graph indicates that an optrode fiber may integrate fluorescence from a similar volume as its flat-cleaved counterpart, despite the curved surfaces in the optical pathway of the optrode. The characteristics of both optrode and flat-cleaved fiber were predicted reasonably by the theoretical model of Zhu and Yappert (1992) (Fig. 4 *B*).

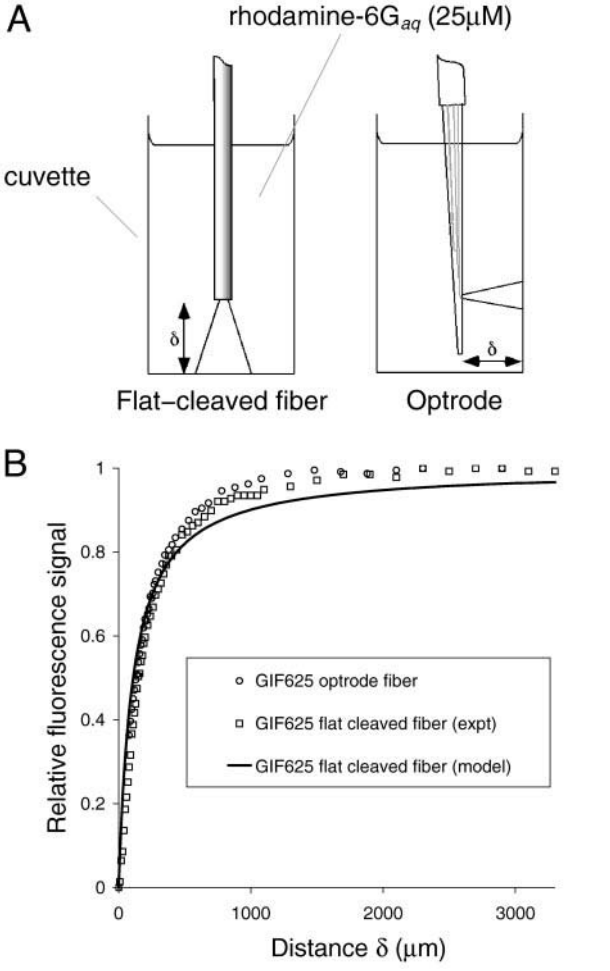

FIGURE 4 (*A*) Schematic showing the experiment to determine the depth collection characteristics of a flat-cleaved fiber, and an optrode fiber. Both were immersed in a fluorescing rhodamine solution contained in a cuvette and moved away from the cuvette boundary in a series of steps. (*B*) Resulting plots of relative fluorescence signal versus depth of fluorescence collection for GIF625 fibers. The experimental measurements for both flat-cleaved fiber and optrode fiber are shown, along with the theoretically derived curve (*solid line*) for the flat-cleaved fiber (Zhu and Yappert, 1992).

System noise

System noise was characterized by varying the fraction of laser power delivered by a single fiber to a fluorescent solution. Signal level was the total fluorescence detected, and the RMS noise on this signal was determined. In Fig. 5, RMS noise is plotted as a function of the mean signal level. The dark noise of the system (RMS noise at zero signal level) was 0.004 mV. The system noise was characteristic of shot noise ($\text{noise}_{RMS} \propto \sqrt{\text{signal}}$) over a small range, before being determined by the laser noise ($\text{noise}_{RMS} \propto$ signal). The fitted line for a laser noise limited system in Fig. 5 indicates RMS laser noise of 0.27% of the signal level. The operating points of the system when using 10 mW of excitation power delivered to the stained heart preparations are shown by white and gray arrows for the 520- to 600-nm and >600-nm wavelength detectors, respectively. The illumination power of 10 mW is similar to that used in the laser scanning optical mapping system of Knisley and Baynham (1997).

Animal experiments

In all rabbit hearts tested, high fidelity membrane potential dependent signals were recorded. Typical raw signals obtained with a combination of both ratiometry and 2,3-BDM (15 mM) are shown in Fig. 6 *A*. Their beat averaged coun-

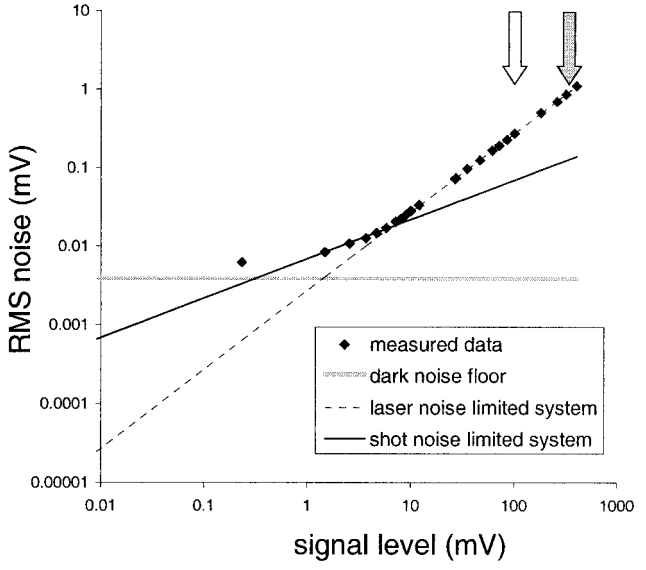

FIGURE 5 Examination of the RMS noise to mean signal level relationship for the optical system (note log-log scale). At high signal levels the system noise becomes dominated by laser noise, and increasing the excitation power to the tissue does little to enhance SNR further. The operating points for 10 mW of excitation power in stained heart tissue are shown by the arrows (*white arrow* for the 520–600-nm detectors and *gray arrow* for the >600-nm detectors).

terparts are shown in Fig. 6 *B*, along with the cardiac electrogram. Time of depolarization was measured in the optical signals by the time at dV/dt_{max} and always lay within the activation complex of the cardiac electrogram. For the recording shown in Fig. 6 activation times had a spread of 6 ms (mean spread was 7.2 ms across all three experiments). Action potential upstroke durations as measured by the time required for the upstroke to change from 10% to 90% of its maximal amplitude were 9.03 ± 1.54 ms (mean ± SD) for Fig. 6 recordings, and 5.82 ± 2.75 ms (mean ± SD; range 1.9–11.52 ms) over all recordings from the three experiments. Typically upstrokes were fastest in the early stages of an experiment (data not shown). Baseline drift in the ratioed signals was 0.4 ± 0.47% per second of recording (mean ± SD), whereas the action potential upstroke constituted 1.86 ± 0.88% of the ratio (mean ± SD) over all experiments. For the analyzed experiments the central fiber of the optrode was not used in recording.

Where 2,3-BDM was not added to the perfusate, the nonratioed voltage-dependent signals were lost within large motion-related signal fluctuations (Fig. 7 *A*). The ratioing of these signals yielded visible action-potential upstrokes that could be identified by their fast rate of rise and their timing relative to the cardiac electrogram. However, the signals still contained large motion artifacts (Fig. 7 *B*). Where 2,3-BDM was added to the perfusate, the nonratioed signals again contained visible motion artifact (Fig. 7 *C*). Ratioing these signals (Fig. 6) appeared to eliminate motion artifact completely and reduced the level of noise common to all channels, by rejection of the fluctuations in laser power.

The time dependency of signal quality was examined in a single heart and is summarized in Fig. 8. Recordings were

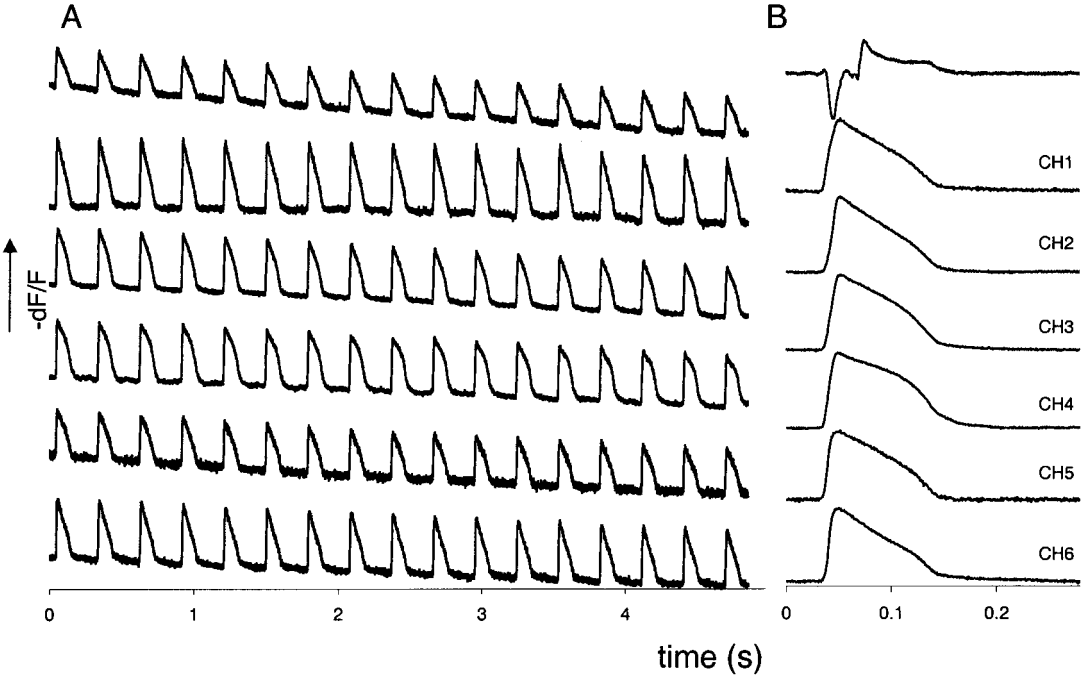

FIGURE 6 (*A*) Raw membrane potential dependent signals obtained with both ratiometry and 2,3-BDM (15 mM). Baseline drift of the signals is on average 78% of the upstroke amplitude over this 5-s recording. (*B*) Upper trace: beat averaged (16 beats) cardiac electrogram recorded close to the optrode. Lower six traces: beat averaged (16 beats) optical signals. Average signal to noise ratios are 42 and 165 for optical signals in *A* and *B*, respectively.

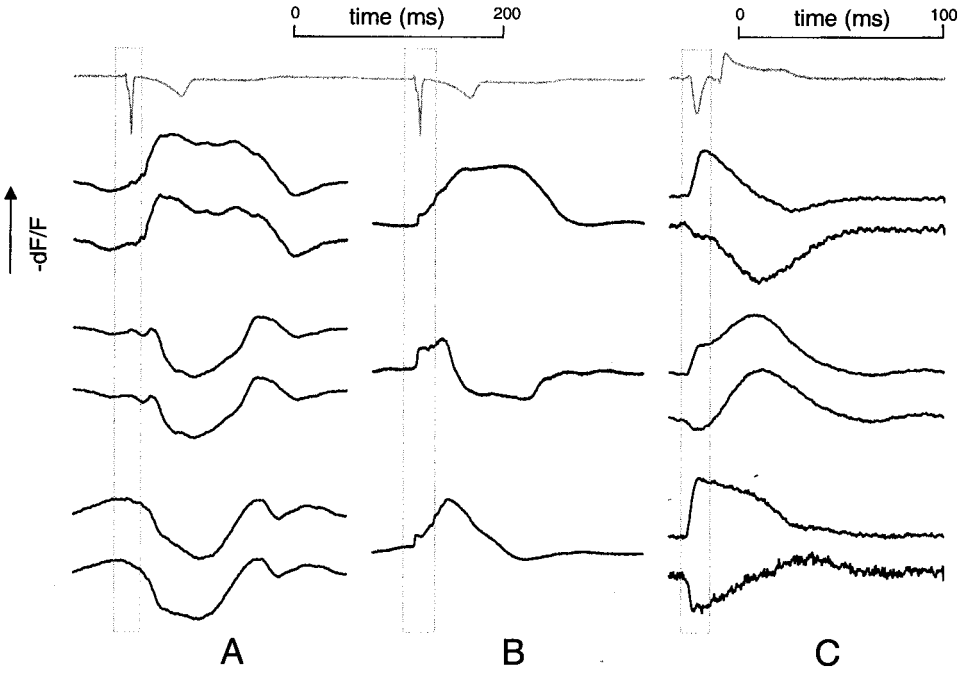

FIGURE 7 All traces represent beat averaged data (16–20 beats). The uppermost (*gray*) traces are cardiac electrograms. (*A*) Lower traces: pairs of optical signals (>600 nm (*top*) and 520–600 nm (*bottom*)) from three optrode recording sites without the addition of 2,3-BDM to the heart. (*B*) Ratioed signals from *A*, showing a clear action potential upstroke followed by substantial motion artifact. (*C*) Pairs of optical signals from three recording sites with 2,3-BDM. Average signal to noise ratios are 47 and 7 for wavelengths > 600 nm and 520 to 600 nm, respectively. See Fig. 6 *B* (CH3-5) for the ratioed signals from *C*.

made from a single optrode that was inserted at three different sites during the course of the experiment. signal to noise ratio (SNR) was calculated as the ratio of action potential amplitude to the RMS noise between action potentials. SNR is plotted against the duration of the experiment, noting the cumulative laser exposure time after each recording. At each optrode insertion site there is a decay in signal quality, this decay being most gradual for the first site.

DISCUSSION

We have shown that it is possible to record high-fidelity membrane potential dependent signals from multiple sites within the heart wall using a fiber-optic based recording system. To obtain reliable signals, uncontaminated by motion-related artifact and light source noise, it was necessary to use a combined approach using both ratiometry and the electro-mechanical decoupling agent 2,3-BDM. Neither approach by itself eliminated motion artifact completely, due to the large degree of movement in the preparation, and the relatively small collection volume of the optical fibers. Ratiometry typically improved SNR 10-fold by rejecting light source noise. The signals obtained by this method have slow baseline drifts of magnitude similar to those reported by Knisley et al. (2000) and signal to noise ratios rivaling those of spatially averaged CCD video recordings of membrane potential from the heart surface (Baxter et al., 1997). Action potentials measured with the optrode typically had upstroke durations that were comparable with those ob-

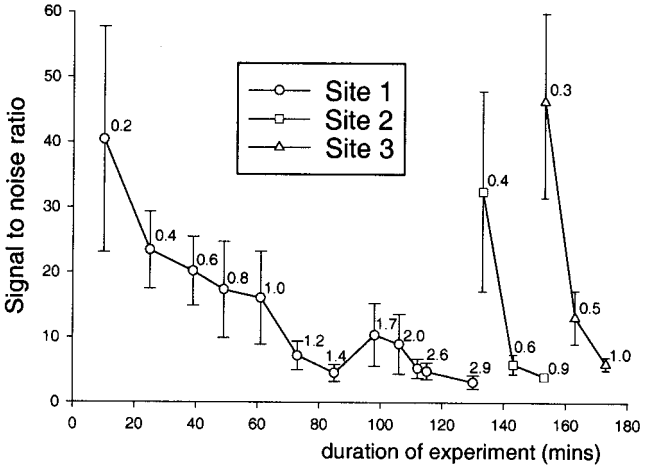

FIGURE 8 Plot of SNR against total duration of the experiment. Data represent the mean and SD of SNR across all six optrode recording channels. The cumulative laser exposure time (min) after each recording is shown alongside each data point. Three optrode placements (sites 1, 2, and 3) were made during the course of the experiment. Total laser exposure of the tissue was 2.9, 0.9, and 1 min at the respective sites. The heart was first stained with di-4-ANEPPS at time zero, then restrained at $t = 90$ min with the optrose left inserted in its first position.

tained with photodiode array based surface optical mapping systems operated at low magnification (surface pixel area of 0.3 mm^2) (Girouard et al., 1996).

To assess the robustness of the recording technique, signal quality was monitored over the course of an experiment. Signals could be recorded for at least an hour at the initial site of optrode insertion. Gradual deterioration of signal quality was observed, which could be attributed to either laser light-induced bleaching of the voltage-sensitive dye or cell death around the optrode or some combination of these factors.

Experiments indicated that there were only slight differences in the fluorescence collection depths of flat-cleaved fibers and their optrode fiber counterparts, indicating that both types of fiber geometry may integrate fluorescence from a similar volume.

Limitations of the present study and recording technique

There are a number of limitations to this study related to both the preparations used, and optical mapping in general. The LV wall thickness of the rabbit hearts was 3 to 4 mm, which did not allow the optrode to be inserted perpendicular to the epicardium. Accordingly, it was not possible to estimate the depth of each fiber tip after insertion, so analysis of transmural differences in action potential morphology is not possible from the present data. Application of the optrode to larger heart experiments will allow such a study as well as the simultaneous introduction of multiple optrodes and/or combinations of optrodes and extracellular plunge electrodes into the LV. Although spreads in activation times among the optrode fibers were seen in all cases, use of a single optrode at any one time did not allow the characterization of a direction of propagation.

Accurate, time-independent calibration of the optical signals in terms of millivolt changes in membrane potential was not possible as evidenced by the slow drift in baseline of the ratioed signals. The reason for this drift was the faster decrease in green emission of the dye compared with red emission, over time, as shown by Knisley et al. (2000).

The fluorescence depth collection characteristics of an optrode fiber were examined in a dilute solution of rhodamine. To what extent the collection depth is altered in the presence of a scattering and absorbing medium such as myocardium is the focus of future investigation.

Extracellular potential mapping

For many decades multisite recording of extracellular potentials was the only tool available to investigate patterns of electrical propagation at the whole heart level. Reconstruction of cellular propagation from extracellular potentials (ϕ_e) relies on the assignment of fiducial markers, within the extracellular recordings, which correspond to cellular activation and recovery at the recording site. Typically the maximal negative slope (intrinsic deflection) of a unipolar recording of ϕ_e is picked as the time of activation (Spach et al., 1972) and the maximal positive slope as the time of repolarization (Steinhaus, 1989). Assignment of these markers to activation and repolarization is based on studies of ideal propagation in uniform domains. Nonideal conditions that introduce errors in the times assigned by the fiducial markers include changes in the uniformity of activation sequence, propagation through regions of nonuniform coupling resistance and/or nonuniform membrane properties, changes in the shape of action potential depolarization and repolarization, and the addition of distant events (Steinhaus, 1989). Under these conditions, errors in estimating repolarization times, in particular, may be large (Steinhaus, 1989). Attempts have been made to use more of the shape information contained within an extracellular potential recording to determine the parameters of cellular propagation more accurately (Di Persio and Barr, 1987; Ganapathy et al., 1985; Spach et al., 1979; Ellis et al., 1996). The disadvantage of these approaches is that they rely on a priori knowledge of tissue parameters such as action potential shape and electrode to tissue distance, together with interstitial and intracellular resisitivities. The problem of how best to define cellular events from extracellular recordings remains unresolved. Despite inherent uncertainties, three-dimensional reconstructions of activation have been carried out with extracellular potential recordings, using the intrinsic deflection to mark depolarization at the recording site. Indirect measures of repolarization such as maps of refractory period duration have been used in three-dimensional studies of reentry, in which knowledge of both activation and recovery processes is crucial (Chen et al., 1988).

Optical mapping of transmembrane potential on the heart surfaces

Over the last 20 years, transmembrane potentials on the surface of the heart have been imaged directly by use of voltage-sensitive dyes. Accurate maps of repolarization have been recorded on the heart surfaces (Efimov et al., 1996). In addition, it has been possible to study the electrical effects of defibrillation and pacing. For instance, recent optical mapping studies have demonstrated that inhomogeneities in post-shock transmembrane polarization may lead to defibrillation failure (Efimov et al., 1998), which occurs as a result of reentrant propagation about a shock-induced phase singularity. To date, however, transmural heterogeneities in action potential morphology and repolarization times have not been well characterized. The recent work of Baxter et al. (2001) offers promise of visualization of phase singularities in a transmural sense, although the transillumination technique used suffers limitations with respect to both spatial resolution and signal quality, particularly in

thick ventricular preparations. It has been shown in modeling studies that phase singularities induced by shocks from implantable cardioverter defibrillators may also occur in the midmyocardium and as filaments in three dimensions, with orientations dependent on the local tissue architecture (Entcheva et al., 1998). Routine experimental visualization of such processes in three dimensions would represent a major advance in cardiac electrophysiology.

Optical mapping with fiber optics

Our optical recording system is based around the use of fiber-optics to deliver excitation light to and collect fluorescence from the tissue, with the principle aim of extending optical recordings of transmembrane potential to sites within the heart wall. Previous use of fiber-optics in the measurement of cardiac action potentials is documented (Krauthamer et al., 1991, 1994; Neunlist et al., 1992). These investigators used single optical fibers to measure voltage-dependent fluorescence signals on the heart surfaces. Such an approach enables the heart to be placed remotely from the recording apparatus but compromises one of the principal benefits of optical mapping, namely the absence of hardware devices contacting the myocardium. The greatest advantage of using fiber optics is the potential to make intramural optical measurements and hence move a step closer to three-dimensional reconstructions of membrane potential. For such measurements to be made, a robust, implantable, multi-fiber optical probe was required.

Optical mapping with large numbers of optical fibers requires efficient coupling of the excitation light source into the fiber-optics to deliver reasonable excitation power to many tissue sites simultaneously. This presents a problem when small diameter fibers are used. Of the optrode fibers compared in this study, the optimal efficiency of the excitation pathway was greatest (26%) for the F-MCB-T fibers. (Because of its hard polymer cladding, the F-MCB-T fiber is also stronger than the GIF625 fiber.) Based on 10 mW of excitation power at each optrode fiber site and seven fibers per optrode, the maximal number of optrodes that could be used with a 5-W laser is 18. Similar numbers of plunge electrodes have been used in three-dimensional extracellular mapping studies (Frazier et al., 1988; Arnar et al., 1997). The optical equivalents of these studies will usefully complement the extracellular potential data already available.

In summary, a novel method for obtaining high-fidelity intramural recordings of transmembrane potential has been developed. We intend to use this system to map transmembrane potential directly in three-dimensional volumes of myocardium. The benefits include direct assessment of propagation without extrapolation from extracellular potential data and the ability to carry out studies into the three-dimensional effects of defibrillation.

We thank Professor Mark Cannell, Dr. Christian Soeller, and Dr. David Wardle who provided helpful comments and advice throughout the duration of this study, and we thank Dean Tai for technical assistance.

This work was funded by the Health Research Council of New Zealand and the Auckland University Research Committee. Darren Hooks is grateful for the support of Maurice and Phyllis Paykel Trust and University of Auckland Doctoral Scholarships.

REFERENCES

Arnar, D. O., J. R. Bullinga, and J. B. Martins. 1997. Role of the Purkinje system in spontaneous ventricular tachycardia during acute ischemia in a canine model. *Circulation.* 96:2421–2429.

Baxter, W. T., J. M. Davidenko, L. M. Loew, J. P. Wuskell, and J. Jalife. 1997. Technical features of a CCD video camera system to record cardiac fluorescence data. *Ann. Biomed. Eng.* 25:713–725.

Baxter, W. T., S. F. Mironov, A. V. Zaitsev, J. Jalife, and A. M. Pertsov. 2001. Visualizing excitation waves inside cardiac muscle using transillumination. *Biophys. J.* 80:516–530.

Chen, P-S., P. D. Wolf, E. G. Dixon, N. D. Danieley, D. W. Frazier, W. M. Smith, R. E. Ideker. 1988. Mechanism of ventricular vulnerability to single premature stimuli in open-chest dogs. *Circ. Res.* 62:1191–1209.

Di Persio, D. A., and R. C. Barr. 1987. A prototype inverse solution in one-dimension to find the origin of excitation, strand radius, intracellular resistivity, or distance from the surface. *IEEE Trans. Biomed. Eng.* 34:681–691.

Durrer, D., and L. H. van der Tweel. 1953. Spread of activation in the left ventricular wall of the dog. I. *Am. Heart J.* 683–691.

Efimov, I. R., Y. Cheng, D. R. Van Wagoner, T. Mazgalev, and P. J. Tchou. 1998. Virtual electrode-induced phase singularity: a basic mechanism of defibrillation failure. *Circ. Res.* 82:918–925.

Efimov, I. R., B. Ermentrout, D. T. Huang, and G. Salama. 1996. Activation and repolarisation patterns are governed by different structural characteristics of ventricular myocardium: experiental study with voltage-sensitive dyes and numerical simulations. *J Cardiovasc. Electrophysiol.* 7:512–530.

Ellis, W. S., S. J. Eisenberg, D. M. Auslander, M. W. Dae, A. Zakhor, and M. D. Lesh. 1996. Deconvolution: a novel signal processing approach for determining activation time from fractionated electrgrams and detecting infarcted tissue. *Circulation.* 94:2633–2640.

Entcheva, E., J. Eason, I. R. Efimov, Y. Cheng, R. Malkin, and F. Claydon. 1998. Virtual electrode effects in transvenous defibrillation-modulation by structure and interface: evidence from bidomain simulations and optical mapping. *J. Cardiovasc. Electrophysiol.* 9:949–961.

Frazier, D. W., W. Krassowska, P-S. Chen, P. D. Wolf, N. D. Danieley, W. M. Smith, and R. E. Ideker. 1988. Transmural activations and stimulus potentials in three-dimensional anisotropic canine myocardium. *Circ. Res.* 63:135–146.

Girouard, S. D., K. R. Laurita, and D. S. Rosenbaum. 1996. Unique properties of cardiac action potentials recorded with voltage-sensitive dyes. *J. Cardiovasc. Electrophysiol.* 7:1024–1038.

Kerber, R. E., K. T. Spencer, M. J. Kallok, C. Birkett, R. Smith, D. Yoerger, and R. A. Kieso. 1994. Overlapping sequential pulses: a new waveform for transthoracic defibrillation. *Circulation.* 89:2369–2379.

Knisley, S. B., and T. C. Baynham. 1997. Line stimulation parallel to myofibers enhances regional uniformity of transmembrane voltage changes in rabbit hearts. *Circ. Res.* 81:229–241.

Knisley, S. B., R. K. Justice, W. Kong, and P. L. Johnson. 2000. Ratiometry of transmembrane voltage-sensitive fluorescent dye emission in hearts. *Am. J. Physiol. Heart Circ. Physiol.* 279:H1421–1433.

Krauthamer, V., H. J. Bryant, C. C. Davis, and T. W. Athey. 1991. Action potential-induced fluorescence changes resolved with an optical fiber carrying excitation light. *J. Fluorescence.* 1:207–213.

Krauthamer, V., C. C. Davis, and E. Gan. 1994. Two-point electrical-fluorescence recording from heart with optical fibers. *IEEE Trans. Biomed. Eng.* 41:1191–1195.

Neunlist, M., S. Zou, and L. Tung. 1992. Design and use of an "optrode" for optical recordings of cardiac action potentials. *Pflugers Arch.* 420: 611–617.

Rohr, S., and J. P. Kucera. 1998. Optical recording system based on a fiber optic image conduit: assessment of microscopic activation patterns in cardiac tissue. *Biophys. J.* 75:1062–1075.

Sands, G., D. A. Hooks, I. J. LeGrice, and B. H. Smaill. 1999. Three dimensional spread of electrical activity in ventricular myocardium. *FASEB J.* 13:A1075.

Selvester, R. H., W. L. Kirk, Jr., and R. B. Pearson. 1970. Propagation velocities and voltage magnitudes in local segments of dog myocardium. *Circ. Res.* 27:619–629.

Spach, M. S., R. C. Barr, G. A. Serwer, J. M. Kootsey, and E. A. Johnson. 1972. Extracellular potentials related to intracellular action potentials in the dog purkinje system. *Circ. Res.* 30:505–519.

Spach, M. S., W. T. Miller, E. Miller-Jones, R. B. Warren, and R. C. Barr. 1979. Extracellular potentials related to intracellular action potentials during impulse conduction in anisotropic canine cardiac muscle. *Circ. Res.* 45:188–204.

Steinhaus, B. M. 1989. Estimating cardiac transmembrane activation and recovery times from unipolar and bipolar extracellular electrograms: a simulation study. *Circ. Res.* 64:449–462.

Zhu, Z. Y., and M. C. Yappert. 1992. Determination of effective depth and equivalent pathlength for a single-fiber fluorometric sensor. *Appl. Spectrosc.* 46:912–918.